

# Systematic biases in parameter estimation of binary black-hole mergers

Tyson B. Littenberg,<sup>1,2</sup> John G. Baker,<sup>2</sup> Alessandra Buonanno,<sup>1</sup> and Bernard J. Kelly<sup>3,4</sup>

<sup>1</sup>*Maryland Center for Fundamental Physics & Joint Space-Science Institute,  
Department of Physics, University of Maryland, College Park, MD 20742*

<sup>2</sup>*Gravitational Astrophysics Laboratory, NASA Goddard Spaceflight Center,  
8800 Greenbelt Rd., Greenbelt, MD 20771*

<sup>3</sup>*Department of Physics, University of Maryland,  
Baltimore County, 1000 Hilltop Circle, Baltimore, MD 21250*

<sup>4</sup>*CRESST & Gravitational Astrophysics Laboratory,  
NASA Goddard Spaceflight Center, 8800 Greenbelt Rd., Greenbelt, MD 20771*

(Dated: September 21, 2012)

Parameter estimation of binary-black-hole merger events in gravitational-wave data relies on matched filtering techniques, which, in turn, depend on accurate model waveforms. Here we characterize the systematic biases introduced in measuring astrophysical parameters of binary black holes by applying the currently most accurate effective-one-body templates to simulated data containing non-spinning numerical-relativity waveforms. For advanced ground-based detectors, we find that the systematic biases are well within the statistical error for realistic signal-to-noise ratios (SNR). These biases grow to be comparable to the statistical errors at high signal-to-noise ratios for ground-based instruments (SNR  $\sim 50$ ) but never dominate the error budget. At the much larger signal-to-noise ratios expected for space-based detectors, these biases will become large compared to the statistical errors but are small enough (at most a few percent in the black-hole masses) that we expect they should not affect broad astrophysical conclusions that may be drawn from the data.

PACS numbers:

## I. INTRODUCTION

Binary black hole (BBH) coalescences are cornerstone sources for gravitational-wave (GW) detectors, be they existing ground-based detectors like LIGO [1] and Virgo [2], planned space-based detectors such as classic LISA [3] or eLISA [4], or a pulsar timing array [5]. The analysis of GW data to detect and characterize binary-black-hole merger events and to test the predictions of general relativity requires some family of efficiently computable signal models, representing all the possible waveforms consistent with general relativity.

Modeling BBH waveforms has historically been separated into three regimes, divided by the different computational procedures suitable for each. The “inspiral” where the individual black holes are sufficiently separated for the post-Newtonian (PN) expansion to be valid [6–9], the “merger” of the binary where numerical relativity (NR) is needed [10–12], and the “ringdown” phase of a single, post-merger, perturbed object relaxing to a Kerr black hole [13, 14].

During the last years, the work at the interface between analytical and numerical relativity has provided the community with a variety of semi-analytical inspiral-merger-ringdown waveform sets [15–26] of varying scope in parameter range and accuracy. These waveforms have already been used to search for GWs from high-mass [27] and intermediate-mass [28] binary black holes in LIGO and Virgo data and also to carry out preliminary parameter estimation studies for ground-based detectors [29] and space-based detectors, such as classic LISA [30, 31]. In this paper we shall study a set of inspiral-merger-

ringdown waveforms based on the Effective-One-Body (EOB) framework [32–36].

Template waveforms will always be an approximation to the true signals and the difference, if large enough, can bias inferences made from the GW data about the astrophysical parameters of the system or the validity of general relativity. Estimates of the systematic errors introduced by waveform approximants in the literature [25, 37–41] have focused only on the inspiral or used general conservative criteria to determine when the waveform has a bias, never using the parameter-estimation techniques employed in actual data analysis.

In this work, we will carry out the first *measurement* of systematic biases introduced when determining the physical parameters of a BBH merger by using EOB waveforms as templates. We do so by simulating data that contain NR waveforms as the “signal” to be detected. Then, using the Markov Chain Monte Carlo (MCMC) method [42, 43], we sample the posterior distribution function for the binary parameters using EOB waveforms as the templates. The characteristic width of the posterior as determined by the MCMC is taken as the *statistical* error, while the distance in parameter space between the dominant mode of the posterior and the true, or “injected” waveform parameters is the *systematic* error, or bias, introduced by these waveforms. We study several different BBH systems, sampling the total mass, mass ratio, and signal-to-noise ratio (SNR) space for both a LIGO/Virgo network in the advanced detector era and a LISA-like configuration.

For this first analysis we employ non-spinning waveforms for quasi-circular orbits. In particular, for the injected signals, we consider the NR waveforms produced

by the Caltech-Cornell-CITA collaboration in Ref. [44]. For the templates we use the EOB waveforms that were calibrated in Ref. [25] to those NR waveforms [44]. Because our emphasis is on BBHs, and the merger waveforms in particular, it is certainly the case that spin magnitude and orientation play an important role in the waveform and parameter estimation [45–49]. NR waveforms with spins aligned or anti-aligned with the orbital angular momentum are available, and EOB waveforms that include spins have been developed in Refs. [22, 26, 36]. However, the spinning EOB waveforms are currently restricted to the dominant mode and additional code development is needed before they can be employed in stochastic sampling methods like the MCMC. Thus, we leave to the future the extension of this study to spinning BBHs.

Within these limitations, we show that the EOB waveforms developed in Ref. [25] and tested here are accurate enough to introduce little-to-no significant biases when the data contain NR waveforms at SNRs consistent with expectations for likely LIGO/Virgo detections ( $\text{SNR} \lesssim 50$ ). For LISA-like detections, where the expected SNRs are much higher than for ground-based detectors, significant biases do emerge. Nonetheless, we find that the discrepancies between the true and measured parameters, at a few percent for the black-hole masses, are small enough to not impact key astrophysical conclusions that may be drawn from the data (e.g., black-hole seed models, etc.) [4, 50, 51]. However, when very high accuracies are required, as when testing the validity of general relativity [52, 53], best-fit EOB waveforms from the existing model will leave behind significant residual power, making them ill suited for these applications without further development.

The remainder of the paper is organized as follows. In Sec. II we describe the numerical and analytic waveforms used in this work. In Sec. III we lay out how the study will proceed, describing in particular the MCMC sampler that we use. We then discuss in detail the results for stellar-mass BBHs in ground-based detectors (Sec. IV) and super-massive BBHs in space-based observatories (Sec. V). In Sec. VI we summarize the findings from this work, address limitations, and discuss future directions to be pursued.

## II. INSPIRAL-MERGER-RINGDOWN WAVEFORMS USED IN THE ANALYSIS

Our study involves comparisons between two sets of waveforms. We primarily seek to *evaluate* a continuously parametrizable family of model waveforms based on the EOB framework, against a discrete set of highly accurate numerical relativity (NR) waveforms. In analogy with observational algorithm tests, we can think of the numerical waveforms as “injected” signals, which we challenge the “template” EOB waveforms to match.

We employ as injected signals the non-spinning NR

waveforms produced by the Caltech-Cornell-CITA collaboration [44], using the spectral Einstein code. The NR polarizations have mass ratio  $q \equiv m_1/m_2 = 1, 2, 3, 4, 6$  and contain  $-2$  spin-weighted spherical harmonics  $(\ell, m) = (2, \pm 2), (2, \pm 1), (2, 0), (3, \pm 3), (3, \pm 2), (4, \pm 4), (5, \pm 5),$  and  $(6, \pm 6)$ . These waveforms provide 30–40 GW cycles before merger, depending on the mass ratio.

The phase and amplitude errors of the NR waveforms vary with mass ratio and gravitational mode. The numerical errors grow toward merger and ringdown, and typically at merger, for the dominant  $(2, 2)$  mode, the phase error ranges between 0.05 and 0.25 rad, while the fractional amplitude error is at most 1%. The subdominant modes can have somewhat larger errors, especially the  $(3, 3)$  and  $(4, 4)$  modes.

Applying the numerical waveforms to generate mock signal observations, we will test the ability of a previously published family of template waveforms to characterize these signals [25]. These template waveforms are based on the EOB framework, founded on the very accurate results of PN theory, an expansion of general-relativity dynamics in polynomials in  $v/c$ . In the EOB approach, however, the PN expansions are applied in a resummed form that maps the dynamics of two compact objects into the dynamics of a reduced-mass test particle moving in a deformed Kerr geometry [32–36]. Waveforms in the EOB formalism are derived from such particle dynamics up to the light-ring (unstable photon orbit) radius. The subsequent ringdown portion of the waveforms is a superposition of quasinormal modes matched continuously to the inspiral. Tunable parameters effectively standing in for currently unknown higher-order PN terms are fixed by matching to numerical relativity simulation results.

The comparable-mass NR waveforms in Ref. [44] were used, together with the small-mass-ratio waveforms produced by the Teukolsky code in Ref. [54], to calibrate a non-spinning EOB model in Ref. [25]. More specifically, the numerical waveforms available at discrete points in the parameter space were employed to fix a handful of EOB adjustable parameters entering the EOB conservative dynamics and gravitational modes. These adjustable parameters were then interpolated over the entire mass-ratio space. The EOB model in Ref. [25] contains four subdominant gravitational modes,  $(2, \pm 1), (3, \pm 3), (4, \pm 4)$  and  $(5, \pm 5)$ , beyond the dominant mode  $(2, \pm 2)$ .

The EOB model in Ref. [25] has been coded in the (public) LIGO Algorithm Library (LAL) [55] (under the name EOBNRv2). We carry out our study using LAL to generate template waveforms. Henceforth, we denote the EOB model with only the dominant  $(2, 2)$  mode as EOB<sub>22</sub>, and the model that includes the four subdominant modes  $(2, \pm 1), (3, \pm 3), (4, \pm 4)$  and  $(5, \pm 5)$  as EOB<sub>HH</sub>.

The phase difference of the  $(2, 2)$  mode between the calibrated EOB model and numerical simulation remains below  $\sim 0.1$  rad throughout the evolution for all mass

ratios considered; the fractional amplitude difference at merger of the (2, 2) mode is 2% and grows to 12% during the ringdown. Around merger and ringdown, the phase and amplitude differences of the subdominant modes between the EOB and NR waveforms are somewhat larger than the ones of the (2, 2) mode. [The numerical errors, and phase and amplitude differences between the EOB and NR waveforms can be read from Figs. 6–10 in Ref. [25].]

To quantify how these differences between template and signal would affect GW searches in Advanced LIGO, Ref. [25] studied the effectualness and measurement accuracy of the EOB model. When investigating the effectualness for detection purposes, they found that the NR polarizations containing the strongest seven modes have a maximum mismatch of 7% for stellar-mass BBHs, and 10% for intermediate-mass BBHs, when only the EOB (2, 2) mode is included for  $q = 1, 2, 3, 4, 6$  and binary total masses 20–200 Hz. However, the mismatches decrease when all the four subdominant EOB modes are taken into account reaching an upper bound of 0.5% for stellar-mass BBHs, and 0.8% for intermediate-mass BBHs. Thus, the EOB model developed in Ref. [25] is accurate enough for detection, which generally requires a mismatch not larger than 7%.

To understand whether the EOB model developed in Ref. [25] is precise enough for measurement purposes, the authors carried out a preliminary study, adopting as accuracy requirement for measurement the one proposed in Refs. [40, 41]. Using a single Advanced LIGO detector, Ref. [25] computed the SNRs below which the EOB polarizations are accurate enough that systematic biases are smaller than statistical errors. Since subdominant modes have non-negligible contribution for large mass ratios, and those modes have the largest amplitude errors, they found that the upper-bound SNRs are lower for the most asymmetric systems, such as  $q = 6$ . However, as stressed in Ref. [25], the accuracy requirement in Ref. [40, 41] may be too conservative and by itself it does not say which of the binary parameters will be biased and how large the bias will be. It could turn out that the biased parameters have little relevance in astrophysics or tests of general relativity. It is the main goal of this paper to measure the actual biases of the EOB model with and without the subdominant modes.

Our study is restricted to binary systems moving along quasi-circular orbits where the spin of each constituent black hole is negligible, thus reducing the model parameters  $\theta$  from a space of 17 dimensions to 9 dimensions:

$$\theta = \{\ln M, \ln \mathcal{M}, \ln D_L, t_p, \sin \delta, \alpha, \cos \iota, \psi, \varphi_p\}. \quad (1)$$

In the above equation,  $M \equiv (1+z)(m_1+m_2)$  is the redshifted total mass of the binary, and  $\mathcal{M} \equiv \nu^{3/5} M$  is its chirp mass, where  $\nu \equiv m_1 m_2 / (m_1 + m_2)^2 = q / (1+q)^2$  is the symmetric mass-ratio. We denote by  $D_L$  the luminosity distance, which, along with the right ascension  $\alpha$  and declination  $\delta$ , describes the location of the bi-

nary. The orientation of the binary's orbital angular-momentum vector  $\hat{\mathbf{L}}$  with respect to the line of sight  $\hat{\mathbf{k}}$  from the observer is encoded in the model using the inclination  $\iota$ , polarization angle  $\psi$ , and phase  $\varphi_p$  — the Euler angles that describe the rotation from  $\hat{\mathbf{k}}$  to  $\hat{\mathbf{L}}$ . The parameter  $t_p$  is the time of the (2, 2) mode's maximum amplitude, when the phase is  $\varphi_p$ .

Our comparisons between the EOB waveforms and the NR data are restricted to the late-inspiral, merger and ringdown, that is roughly 30–40 GW cycles before merger, depending on the mass ratio. The injected signals contain only the NR waveforms available. We do not match the NR waveforms to EOB or PN waveforms at low frequency to increase the number of cycles because we do not know how well the EOB or PN waveforms would approximate the NR waveforms outside the region of calibration and we do not want to introduce unknown errors when estimating the systematic biases.

There is no guarantee that a template that is in phase with the NR waveform during the last 30–40 GW cycles will remain so throughout the entire inspiral. The mass parameters are strongly encoded in the GW phase, so any additional de-phasing at earlier times than covered by the NR simulations can potentially increase the systematic biases. Therefore, in order for our study to be meaningful, we consider binary systems that have a total mass such that the majority of the SNR is accumulated during the last 30–40 GW cycles before merger.

### III. STATISTICAL VERSUS SYSTEMATIC ERRORS USING MCMC TECHNIQUES

We use the MCMC algorithm [42, 43] to produce samples from the posterior distribution function for the waveform parameters. The MCMC sampler is built on the foundation of Bayes' Theorem, which, in the context of parameter inference, defines the posterior distribution function for parameter vector  $\theta$  and data  $d$  as

$$p(\theta|d, \mathcal{I}) \equiv \frac{p(d|\theta, \mathcal{I})p(\theta|\mathcal{I})}{p(d|\mathcal{I})}. \quad (2)$$

Here  $p(\cdot|\cdot)$  are conditional probability densities with arguments on the right-hand side of the bar assumed to be true,  $p(d|\theta, \mathcal{I})$  is the likelihood,  $p(\theta|\mathcal{I})$  is the prior distribution, and  $p(d|\mathcal{I})$  is the model evidence, which, in parameter-estimation applications, serves only as a normalization constant. The information  $\mathcal{I}$  denotes all of the assumptions that are built into the analysis, particularly that the NR waveforms represent reality (see Sec. II for associated discussion). Henceforth, to simplify notation, we shall not include  $\mathcal{I}$  when writing the conditional probability density  $p(\cdot|\cdot)$ . When comparing different model combinations, we adopt the notation for conditional probabilities with arguments to the right of a vertical bar representing the data and arguments to the left signifying which model was used as templates.

For example, results labeled  $p(\text{EOB}_{22}|\text{NR})$  come from the posterior distribution functions for models using  $\text{EOB}_{22}$  as the templates and an NR waveform as the data.

With the posteriors, we compare the statistical error (the characteristic width of the posterior) to the systematic error (the displacement from the injected parameter values of the posterior’s mode). We do not include a noise realization in the simulated data, as that introduces additional biases – each noise realization pushing the best-fit solution away from the injected value in a different way — which are not easily quantified [56]. As the control in this experiment, we simulated (noise-free) data with EOB waveforms and use EOB templates for parameter estimation, giving us one set of results with no systematic bias except from the sampling error in the Markov chains due to their finite length. We use these controlled results as code verification, and as the standard against which the other models’ performance is compared. We then test the EOB waveform models by injecting NR waveforms (summed over all available modes) and using the two EOB models discussed in Sec. II as templates. The  $\text{EOB}_{22}$  model is used as a baseline, as it has been employed in LIGO/Virgo search pipelines to analyze data collected in recent science runs [28, 57]. The  $\text{EOB}_{\text{HH}}$  model is the most complete waveform at our disposal and is used to measure how well the EOB model could perform on NR data.

In Eq. (2) we use the standard gaussian logarithmic likelihood  $\ln p(d|\theta) \equiv -(d - h(\theta)|d - h(\theta))/2 + C$ , where  $C$  is a normalization constant that does not depend on model parameters and is henceforth neglected,  $h$  is the template, and

$$(a|b) \equiv 2 \sum_{i=1}^I \int_{f_{\min}}^{f_{\text{Nyq}}} \frac{\bar{a}_i^*(f)\bar{b}_i(f) + \bar{a}_i(f)\bar{b}_i^*(f)}{S_n^i(f)} df, \quad (3)$$

denotes a noise-weighted inner product with the sum on  $i$  over  $I$  (independent) interferometer channels and  $S_n^i(f)$  is the one-sided noise power spectral density (PSD) for detector  $i$ . The bounds of integration  $[f_{\min}, f_{\text{Nyq}}]$  are the minimum frequency of the NR waveform and the Nyquist frequency of the data, respectively. The Nyquist frequency is chosen to ensure that the highest frequency portion of the waveform is well below the instrument sensitivity curve, while  $f_{\min}$  is set by the duration of the NR waveform and the total mass of the system, such that we only integrate over frequencies where there is numerical data.

For each case, the Markov chains are run for  $\sim 10^6$  iterations, taking about  $10^3$  CPU hours to complete. The chains rely on parallel tempering [58], differential evolution [59], and jumps along eigenvectors of the FMI (e.g., see Ref. [60]) computed from PN waveforms to efficiently explore the posterior distribution function. We use burn-in times of  $10^4$  samples, and run several chains with different initial locations to check for convergence. Prior distributions for all parameters are chosen to be uniform. Azimuthal angular parameters ( $\alpha$ ,  $\psi$ , and  $\varphi_p$ ) have support over  $[0, 2\pi)$  with periodic boundary conditions, while

declination-like angle parameters ( $\sin \delta$ ,  $\cos \iota$ ) range from  $[-1, 1]$  with reflecting boundary conditions. The ranges for  $\ln M$  and  $\ln D_L$  are chosen to be large enough so as to not influence the posteriors. The prior range on  $\ln \mathcal{M}$  is coupled to  $\ln M$ , as the maximum value of the chirp mass occurs for the  $q = 1$  ( $\nu = 1/4$ ) case, and depends on the total mass  $M$  of the system. Because of this, the prior boundary on chirp mass does affect the posteriors for the equal-mass systems considered in this work.

The products of our analysis procedure are samples from the posterior distribution function  $p(\theta|d)$  — an oddly shaped, sometimes multimodal, blob living in a 9D space. There is no perfect way of distilling this information into a simple, robust, statistic to assess parameter-estimation accuracy. We will make do with the “fractional systematic error”  $\delta\beta_\theta$ . For parameter  $\theta$ , we first define the systematic error  $\beta_\theta \equiv |\theta_{\text{MAP}} - \theta_0|$  where  $\theta_{\text{MAP}}$  is the *maximum a posteriori* (MAP) value and  $\theta_0$  is the injected value, while the statistical error is quantified by the standard deviation of the 1D marginalized posterior distribution function  $\sigma_\theta$ . We then define the fractional systematic error as the ratio between  $\beta_\theta$  and the statistical error:

$$\delta\beta_\theta \equiv \frac{\beta_\theta}{\sigma_\theta}. \quad (4)$$

We consider templates that consistently yield  $\delta\beta_\theta \lesssim 1$  as introducing negligible bias assuming the NR waveforms are exact, which, as seen in Sec. II, is not the case<sup>1</sup>.

The fractional systematic error (4) can be interpreted as the number of standard deviations away from the injected value at which we find the MAP waveform. This choice of statistic is not perfect — low-SNR systems have very non-gaussian posteriors making the standard deviation a poor choice for characterizing the statistical error. Furthermore, the MAP parameters are a single point and tell us nothing about how large a region in parameter space had similar posterior support to the current best estimate. Additionally, the MAP value is a feature of the full 9D posterior, while the variances are computed from the *marginalized* posterior distribution functions. This introduces complications for some special cases as we shall discuss in detail below.

#### IV. RESULTS FOR ADVANCED LIGO DETECTORS

The first test of the EOB waveforms uses simulated data from the network of advanced ground-based detectors expected to come on line in the middle of this decade: the two LIGO detectors in the USA and the Virgo detector in Italy. We use the same noise PSD for each interferometer, the “zero-detuned high-power” curve from

<sup>1</sup> Currently we have no way of incorporating the numerical error of the NR waveforms into our estimate and so we neglect it.

Ref. [61], which is the sensitivity curve for the fully completed Advanced LIGO detector. The GW response in each interferometer is modeled by convolving the GW signal with the beam-pattern function for that detector and applying the appropriate time-delays between interferometers [62].

### A. Choice of binary configurations

We study several binary configurations using different mass ratios, total masses, and SNRs. The SNR of the system is computed via  $\text{SNR} = \sqrt{\langle d|d \rangle}$ , and its value is controlled by adjusting the luminosity distance  $D_L$ . Because our simulated data  $d$  contain no simulated noise, the SNR is simply the inner product of the injected waveform with itself. Also, our definition of the inner product in Eq. (3) includes a summation over all interferometer channels, thus we quote the *network* SNRs for the ground-based studies.

The first three panels of Fig. 1 show the time-domain  $\text{EOB}_{\text{HH}}$  waveforms (blue, dotted) and whitened by the noise spectral density (red, solid) for three representative cases studied here. The vertical lines indicate intervals in which 10% of the signal power is accrued, starting from  $f_{\text{min}}$  for each system, with the rightmost line indicating where 99.9% of the power has accumulated. The power intervals are included as a guide to see which portions of the waveform contribute most to the parameter estimation. For instance, the  $q = 1$ ,  $M = 50 M_{\odot}$  waveform acquires 50% of the signal power in the last 1000  $M$  of the signal, while the  $q = 2$ ,  $M = 23 M_{\odot}$  signal is much less dominated by the late-inspiral and merger, accounting for only 30% of the power. The  $q = 6$ ,  $M = 120 M_{\odot}$  examples are most influenced by the latter stages of the signal, which make up over 70% of the power.

The bottom-right panel of Fig. 1 shows the strain spectral densities for the same three systems, now using the NR waveforms used in this study. Also included is the Advanced LIGO power spectral density.

We focus on moderately high-mass black-hole mergers with  $M \sim 50 M_{\odot}$  (e.g., the equal-mass case shown in Fig. 1: top-left panel, red solid curve in bottom-right panel). Beyond their potential as Advanced LIGO sources<sup>2</sup>, high-mass systems serve an important role in

testing the waveform models for two reasons: First, as explained in Sec. II, the NR signals are short in duration and we do not supplement the waveform by hybridizing the numerical data with analytic inspiral models at low frequency. We therefore require higher-mass systems, merging at lower frequency, to ensure that most of the inspiral missing from the NR data will fall outside the sensitive measurement band of the detector. With  $M \sim 50 M_{\odot}$  NR waveforms start at  $\sim 30$  Hz, setting  $f_{\text{min}}$  in the inner product defined in Eq. (3). Comparing these data to EOB waveforms with the same parameters but  $f_{\text{min}} = 10$  Hz (below which the Advanced LIGO sensitivity is very poor), we find the NR waveforms contain  $\sim 85\%$  of the total signal power, or  $\sim 90\%$  of the total SNR.

A second reason for focusing on  $M \sim 50 M_{\odot}$  for the binary is that these systems are “centrally located” in frequency over the most sensitive band of the advanced detectors ( $\sim 30$  to  $\sim 10^3$  Hz, e.g., see the bottom-right panel in Fig. 1), such that inspiral, merger, ringdown, and additional modes all contribute to the overall signal power and, accordingly, the parameter-estimation capabilities. Generally speaking, we expect such systems to make the greatest demands on complete inspiral-merger-ringdown waveform model accuracy.

While the  $M \sim 50 M_{\odot}$  systems serve as the basis for our comparisons, we include additional examples to probe regions of signal space that are of particular interest. These include a  $q = 6$ ,  $120 M_{\odot}$  system (Fig. 1: bottom-left panel, blue dotted curve in bottom-right panel) chosen such that the subdominant modes contribute the most, as they will be most pronounced at high mass ratios, and signal power from the higher frequency modes is still in the sensitive band of the detector. At this mass,  $f_{\text{min}} = 10$  Hz, so our analysis is not missing any signal power due to the length of the NR data.

We also go to lower masses, using a  $q = 2$ ,  $23 M_{\odot}$  binary (Fig. 1: top-right panel, green dashed curve in bottom-right panel) as a more likely LIGO/Virgo detection, to demonstrate the EOB models’ parameter-estimation accuracy not at the extremes of a potential binary signal, but within reasonable expectations of what the coming data may hold (apart from including the black-hole spins). It is worth noting that for these low-mass systems we are missing a large portion of the inspiral, as  $f_{\text{min}} = 60$  Hz and  $\sim 30\%$  of the full SNR will be accumulated below that frequency. Therefore, these results might change in the future when longer EOB and NR waveforms become available.

### B. Results on systematic biases at fixed inclination angle

In Fig. 2 we plot the 1D marginalized posterior distribution functions for each parameter for the case of a binary with mass ratio  $q = 2$ , total mass  $M = 51 M_{\odot}$ , and network  $\text{SNR} = 48$  produced using an MCMC sam-

<sup>2</sup> A binary with  $M \sim 50 M_{\odot}$  is astrophysically relevant, as the largest black-hole mass ever observed is in the range of 23–34  $M_{\odot}$  [63, 64]. Recent results from population-synthesis studies suggest that massive, low-metallicity stars are capable of producing black holes as large as  $M \sim 80 M_{\odot}$  [65], although these findings are for single stars only, and binary evolution could either increase or decrease the maximum black-hole mass. Additionally, there exists at least one example of a massive Wolf-Rayet star, R136a1 [66], with  $M \sim 250 M_{\odot}$  at a distance of  $\sim 0.1$  Mpc and with sufficiently low metallicity to produce a massive black hole. However, it cannot be excluded that the star goes instead through a pair-instability supernovae leaving no remnant.

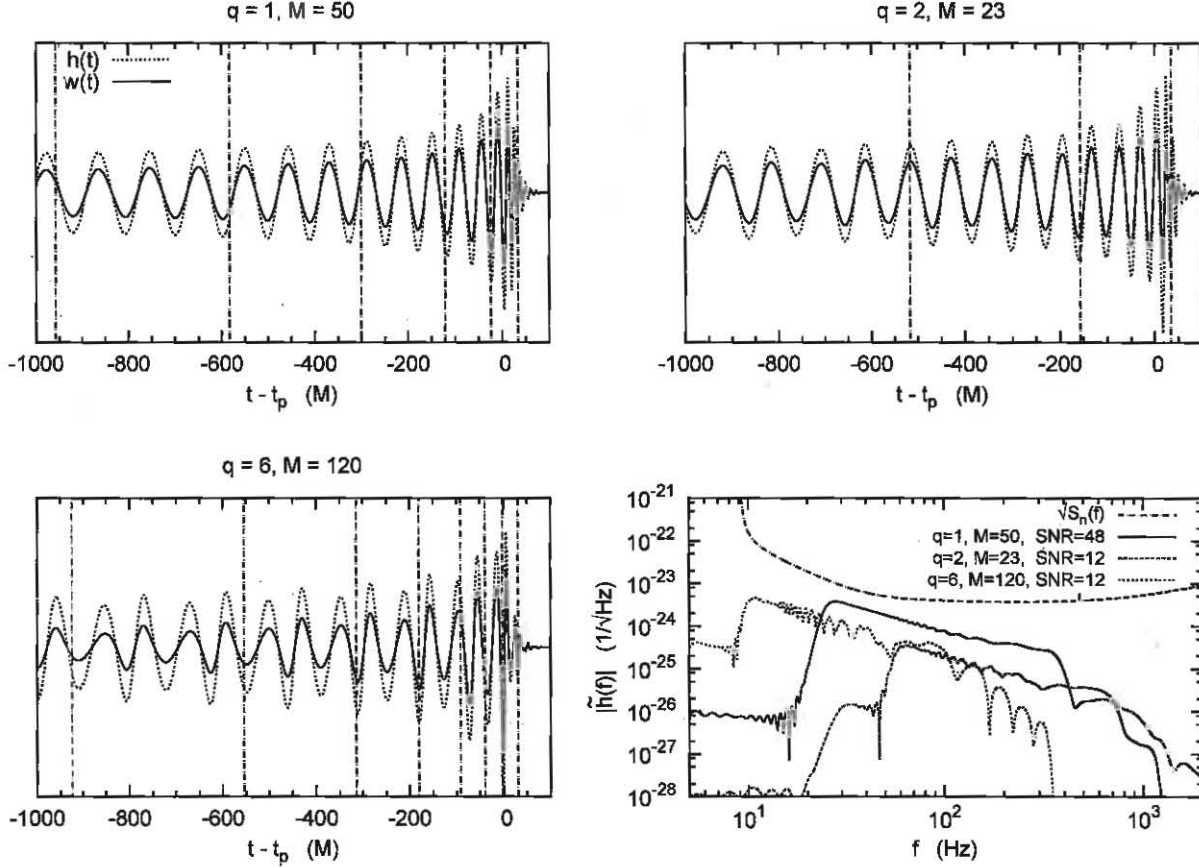


FIG. 1: [Top row, and bottom-left] Time-domain EOB waveforms (blue dotted) and the same signal whitened by the noise spectral density (red solid) representing different test cases studied in this work. The time-axis is scaled by the total mass and shifted by the merger time. The horizontal dotted lines demarcate 10% intervals for accumulated signal power, with the rightmost line at the 99.9% mark. [Bottom right] Strain spectral densities  $|\hat{h}(f)|$  showing the estimate for the Advanced LIGO noise curve (gray dotted line) and the NR waveforms for the same representative examples as the other panels.

pler. The inclination angle is chosen to be  $\iota \sim \pi/3$ . The independent variables in these plots are  $\Delta\theta = \theta - \theta_{\text{inj}}$ , where  $\theta_{\text{inj}}$  are the injected parameter values. The  $p(\text{EOB}_{22}|\text{EOB}_{22})$  histograms (green, dashed lines) are the posteriors using the  $\text{EOB}_{22}$  waveforms for both the signal and the templates. These confirm that the MCMC sampler is working properly, as the posteriors all show strong support for the injected waveform parameters (peaking at or near 0) and statistical errors consistent with results in Ref. [29] obtained using FMI estimates and phenomenological inspiral-merger-ringdown waveforms.

The red (solid) lines and blue (dotted) lines are for data containing an NR signal and the  $\text{EOB}_{22}$  and  $\text{EOB}_{\text{HH}}$  waveforms as templates, respectively. The bottom-right panel shows the logarithmic likelihood distributions for each chain. We can see from these posteriors that the  $\text{EOB}_{22}$  waveform is significantly biased away from the NR injected value, by  $\sim 1\%$  in both  $M$  and  $\mathcal{M}$ . This

bias is substantially reduced when including the subdominant modes in the EOB template, to the point where the systematic error is well within the statistical error of the posterior. For the extrinsic parameters such as distance and sky-location, the posteriors for the approximate templates are nearly identical to those produced by using the exact same waveform for both data simulation and parameter estimation. We also see the role that subdominant modes play in breaking the  $\pi/2$  degeneracy in the polarization angle  $\psi$ , which can aid in distance and sky-location determination for some systems.

The SNR of the residual  $d - h$ , given by  $\text{SNR}_{\text{res}} = \sqrt{-2 \ln p(d|\theta)}$  can be inferred from the bottom-right panel. Viewed in this way, there is a distinct excess in the residual for even the  $\text{EOB}_{\text{HH}}$  case (blue, dotted) in comparison with the idealized control MCMC residuals (green, dashed). To understand the significance of this, consider applying a detection threshold of  $\text{SNR} = 6$  [67] for the residual waveform. This corresponds to a maxi-

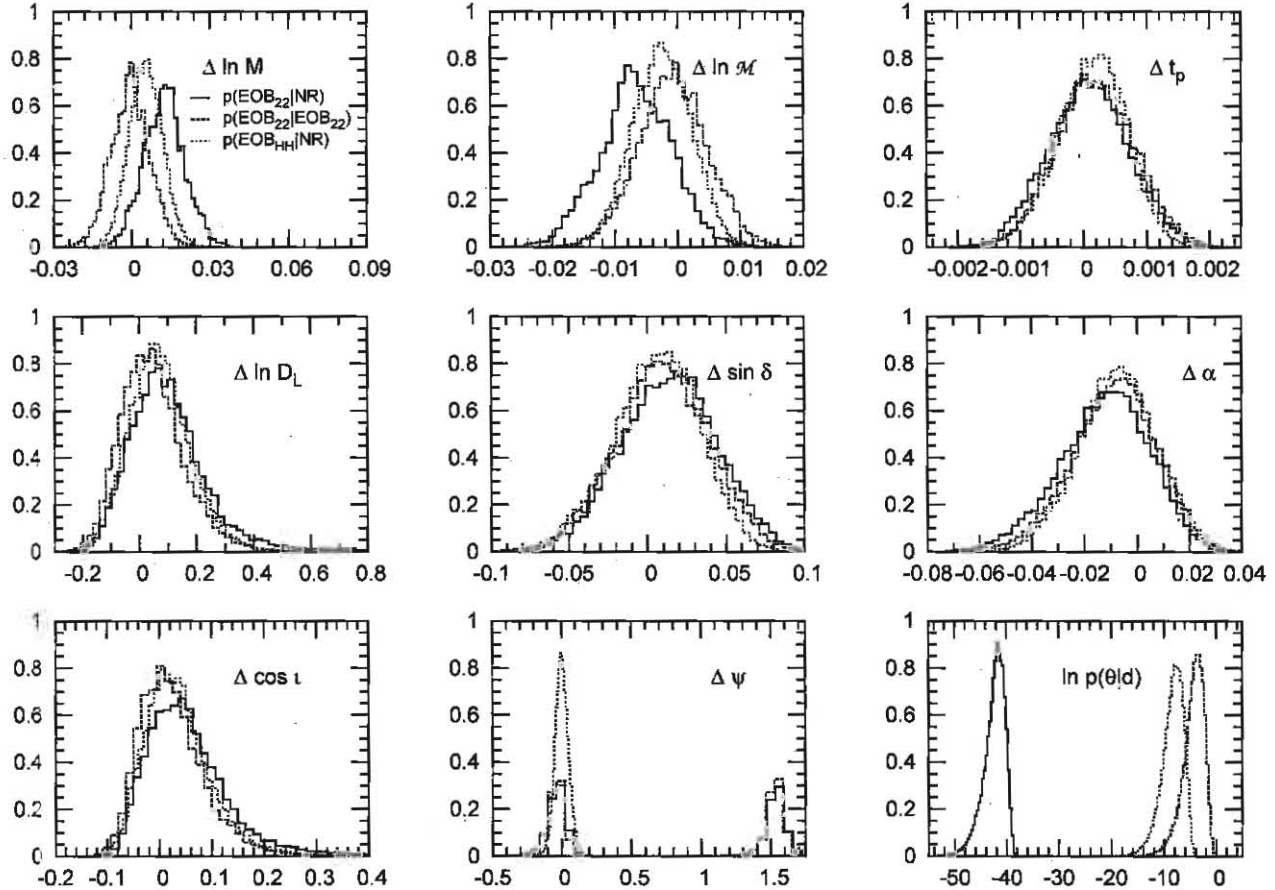


FIG. 2. Example marginalized posterior distribution functions for a binary system with mass ratio  $q = 2$ , total mass  $M = 51M_{\odot}$ , and network SNR = 48 produced using an MCMC sampler. The green (dashed) histograms arise from injecting the EOB<sub>22</sub> waveforms and using the same model as the template. The red (solid) distributions use the EOB<sub>22</sub> waveform while the blue (dotted) curves use the EOB<sub>HH</sub> waveform to recover an NR injection. The  $x$ -axis shows the distance away from the injected parameter value, so distributions that peak at zero show no bias. The bottom-right panel shows the logarithmic likelihood distributions, which are used to quantify the amount of residual power left behind by the waveform model. The  $y$ -axes have been normalized to range between  $[0, 1]$ .

imum logarithmic likelihood of  $\lesssim -18$ , below which the residual could potentially contain enough power to be detected after the best-fit waveform is regressed from the data. Suppose in the near future we have model waveforms at our disposal containing all of the details of black-hole mergers (i.e. spins and eccentricity) that generally produce  $\text{SNR}_{\text{res}} \lesssim 6$  for equally detailed NR simulations, and yet coherent residuals are consistently found in the data. Such an event could suggest a possible departure from general relativity.

The results from our MCMC studies for different systems are displayed in Tables I and II, which show the fractional systematic error  $\delta\beta$  (defined in Sec. III) for the mass, sky location, and distance parameters. The injected waveforms again had an inclination angle of  $\iota = \pi/3$ . We include our estimate of the statistical error  $\sigma_{\theta}$  to quantify the precision of the advanced detectors for the systems considered here. The standard deviations

should be interpreted with caution; we do not include noise in the simulated data, so the deviations are not representative of the “error bars” on a *particular* detection, but instead represent an ensemble average over idealized Gaussian stationary noise realizations of the statistical error for these particular systems.

Table I contains the *intrinsic* parameters — those that affect the shape of the waveform. Because we consider non-spinning black holes, the only intrinsic parameters are the masses. The *extrinsic*, or observer-dependent, parameters (i.e., distance and sky-location) are given in Table II. They are encoded in the instrument response to the GW, instead of being imprinted in the phase and amplitude evolution of the waveform itself. We do not report on the orientation parameters  $\iota$  and  $\psi$  or reference time  $t_p$  and phase  $\varphi_p$  parameters in this fashion, but note that results for these other parameters are consistent with the extrinsic variables in Table II.

$q$	$M$ ( $M_\odot$ )	$f_{\text{low}}$ (Hz)	SNR	$p(\text{EOB} \text{EOB})$				$p(\text{EOB}_{22} \text{NR})$				$p(\text{EOB}_{\text{HH}} \text{NR})$			
				$\sigma_{\ln M}$	$\sigma_{\ln \mathcal{M}}$	$\delta\beta_{\ln M}$	$\delta\beta_{\ln \mathcal{M}}$	$\sigma_{\ln M}$	$\sigma_{\ln \mathcal{M}}$	$\delta\beta_{\ln M}$	$\delta\beta_{\ln \mathcal{M}}$	$\sigma_{\ln M}$	$\sigma_{\ln \mathcal{M}}$	$\delta\beta_{\ln M}$	$\delta\beta_{\ln \mathcal{M}}$
1	50	30	12	0.02	0.02	0.11	0.05	0.02	0.02	0.34	0.17	0.02	0.02	0.29	0.10
1	50	30	48	$4 \times 10^{-3}$	$3 \times 10^{-3}$	$1 \times 10^{-3}$	0.14	0.01	0.01	1.76	0.84	$2 \times 10^{-3}$	$2 \times 10^{-3}$	0.79	0.87
2*	23	60	12	0.02	0.01	0.01	0.02	0.03	0.02	0.27	0.07	0.03	0.02	0.18	0.26
2	51	30	12	0.03	0.02	$3 \times 10^{-3}$	$4 \times 10^{-3}$	0.03	0.02	0.47	0.28	0.03	0.02	0.01	0.01
2	51	30	48	0.01	0.01	0.01	0.01	0.01	0.01	1.92	1.39	0.01	0.01	0.93	0.32
6	56	30	12	0.03	0.03	0.03	0.08	0.03	0.03	0.94	0.66	0.02	0.02	0.58	0.39
6	56	30	48	0.01	$5 \times 10^{-3}$	0.23	0.04	0.01	0.01	3.47	2.51	0.01	$4 \times 10^{-3}$	1.43	0.84
6*	120	10	12	0.03	0.03	0.05	0.14	0.03	0.03	1.67	0.60	0.02	0.02	0.29	0.06

TABLE I: Fractional systematic biases  $\delta\beta$  (see Eq. (4)) and statistical errors  $\sigma$  for intrinsic parameters as determined by the MCMC sampler. An asterisk in the mass ratio column indicates examples where  $\text{EOB}_{\text{HH}}$  was used for the  $p(\text{EOB}|\text{EOB})$  study. All other examples used the  $\text{EOB}_{22}$  waveform.

From Table I we can see that generically, the  $\text{EOB}_{22}$  waveforms are not as accurate as the  $\text{EOB}_{\text{HH}}$  waveforms, which include the subdominant modes. This is true even for comparable-mass systems, where the subdominant modes only minimally contribute to the overall waveform power. The bias introduced by neglecting additional harmonics is not due to missing waveform power as much as it is caused by phase differences between a quadrupole-only template and the full NR data, as coherent matched filtering analysis are typically more sensitive to phase than amplitude.

The parameter estimation accuracy of the  $\text{EOB}_{\text{HH}}$  model up to SNR  $\sim 50$  exceeds expectations from Ref. [25], as can be seen by focusing on rows 2 and 7 in Table I. Here we find systems chosen specifically to compare with Fig. 15 in Ref. [25] where, based on the accuracy requirement proposed in Refs. [40, 41], they predicted that systematic error could exceed statistical error at *single-detector* SNR  $\sim 35$  ( $q = 1$ ,  $M = 50M_\odot$ ) and  $\sim 11$  ( $q = 6$ ,  $M = 56M_\odot$ ).<sup>3</sup>

Our analysis uses the LIGO/Virgo network of detectors, as opposed to the single-detector studies from Ref. [25]. This difference will not heavily impact the results, as it is the measurement of *intrinsic* parameters that is most affected by differences in the waveform model due to both the accuracy with which they are measured, and the way they are encoded in the phase evolution of the signal. Measurement of the intrinsic parameters is not greatly influenced by the inclusion of additional detectors in the network (at a fixed SNR). Our findings show that, even at SNRs that are rather high for an expected LIGO detection, the  $\text{EOB}_{\text{HH}}$  model introduces systematic errors that differ by  $\lesssim 1\sigma$  from the injected parameters.

The extrinsic parameters, on the other hand, are in-

ferred mostly from the overall amplitude of the waveform, which is not as well measured as phase, and the time-of-arrival of the signal at each detector. We thus expect that the extrinsic parameters, determined with lower fidelity than the masses, will be better able to tolerate small differences between template waveform models within the statistical error. Adding additional detectors to the network dramatically improves the statistical error for extrinsic parameters, mostly due to the increased baseline [68], but not to the point of becoming influenced by the waveform systematics.

Indeed, we find that the relative systematic biases for extrinsic parameters are generally smaller than those of the intrinsic parameters. For systems with  $q \geq 2$ , regardless of the SNR or the EOB model, the systematic errors are consistently smaller than the statistical errors, even when the (2, 2)-only waveform is used as the template. This is evident in Fig. 2, where the  $D_L$ ,  $\sin \delta$ , and  $\alpha$  posteriors are nearly indistinguishable, despite the significant difference in the residual left behind by the waveform model, as shown in the bottom-right panel containing the logarithmic likelihood distributions. The same can not be said for the equal-mass cases (top two rows in Table II), where we encounter a subtle effect from our choice of statistic,  $\delta\beta$ .

For the SNR = 12, equal-mass case, the  $\delta\beta$  statistic breaks down and results are omitted from the table. At such a low signal strength, the orientation parameters are very poorly measured, with the polarization angle  $\psi$  effectively unconstrained. These large measurement uncertainties cascade through the 1D posteriors via strong  $\psi - \iota$  and  $\iota - D_L$  covariances. We are left with an unconstrained  $D_L$  distribution that is poorly characterized by the variance, and large stochastic variation from one Markov chain run to the next as to where the MAP parameters lie. This degeneracy is evident in Fig. 3, where we show the 2D marginalized posterior distribution function of the  $\psi - \cos \iota$  plane (left panel) from a  $p(\text{EOB}_{\text{HH}}|\text{NR})$  run, and the maximum logarithmic likelihood found in the Markov chain for different bins in  $D_L$  space (right panel) from both  $p(\text{EOB}_{22}|\text{EOB}_{22})$  and  $p(\text{EOB}_{\text{HH}}|\text{NR})$ . We see a virtually flat distribution of the

<sup>3</sup> The accuracy criterion used in Refs. [25, 40, 41] is a “sufficient” but “not necessary” requirement for parameter estimation, and it does not say which of the binary parameters will be biased and how large the bias will be. Thus, the authors of Ref. [25] were making conservative judgments about the waveform accuracy.

$q$	$M$ ( $M_\odot$ )	$f_{\text{low}}$ (Hz)	SNR	$\sigma_{\sin \delta}$ $\sigma_\alpha$ (rad)		$p(\text{EOB} \text{EOB})$				$p(\text{EOB}_{22} \text{NR})$				$p(\text{EOB}_{\text{HH}} \text{NR})$			
				$\sigma_{\sin \delta}$	$\sigma_\alpha$	$\sigma_{\ln D_L}$	$\delta\beta_{\ln D_L}$	$\delta\beta_{\sin \delta}$	$\delta\beta_\alpha$	$\sigma_{\ln D_L}$	$\delta\beta_{\ln D_L}$	$\delta\beta_{\sin \delta}$	$\delta\beta_\alpha$	$\sigma_{\ln D_L}$	$\delta\beta_{\ln D_L}$	$\delta\beta_{\sin \delta}$	$\delta\beta_\alpha$
1	50	30	12	0.06	0.04	—	—	—	—	—	—	—	—	—	—	—	—
1	50	30	48	0.03	0.01	0.10	0.11	0.01	0.09	0.12	0.12	0.17	0.03	0.20	0.64	0.07	0.30
2*	23	60	12	0.06	0.03	0.24	0.02	0.04	0.02	0.27	0.28	0.02	0.06	0.25	0.30	0.05	0.08
2	51	30	12	0.06	0.04	0.28	0.03	0.08	0.06	0.29	0.21	0.28	0.07	0.27	0.60	0.15	0.33
2	51	30	48	0.03	0.02	0.12	0.10	0.10	0.08	0.14	0.11	0.19	0.11	0.11	0.07	0.04	0.05
6	56	30	12	0.07	0.05	0.29	0.07	0.04	0.21	0.29	0.28	0.14	0.09	0.25	0.40	0.41	0.39
6	56	30	48	0.03	0.02	0.14	0.29	0.10	0.07	0.19	0.28	0.14	0.09	0.09	0.78	0.27	0.21
6*	120	10	12	0.08	0.05	0.21	0.23	0.28	0.13	0.30	0.86	0.37	0.54	0.22	0.36	0.02	0.16

TABLE II: Same as Table I, except here we show a subset of the extrinsic parameters corresponding to the binary’s location. Because of their similarity between each run, the statistical errors are displayed once but apply to each example. Results for the  $q = 1$ , SNR = 12 example are omitted due to the failure of our  $\delta\beta$  statistic.

maximum logarithmic-likelihood values between  $\sim 0.5$  to  $\sim 2.25$  Gpc, with well over half of the allowed parameter space in the  $\psi - \cos \iota$  plane receiving significant posterior support. The injected value of  $D_L$  was near 1 Gpc.

The over-density at  $\{\psi, \cos \iota\} \simeq \{\pi/3, 0.5\}$  corresponds to the injected parameter values, with the  $\pi/2$  - shift degenerate mode still appearing despite the inclusion of subdominant modes. Recall that this is an equal-mass system, where the subdominant modes are the least noticeable. The over-density at  $\cos \iota \sim 1$  is due to the Markov chain preferring template waveforms with minimal contribution from subdominant modes (to match the strictly equal-mass injection) as the sampler explores higher mass ratios, up to  $q \sim 3$  in this case. Systems with  $\cos \iota \equiv \hat{\mathbf{k}} \cdot \hat{\mathbf{L}} = 1$  are face-on and it is this configuration where the subdominant modes are least prominent.

### C. Dependence of the results on the inclination angle

Due to the high computational cost of each MCMC run, we are not able to Monte Carlo over a large population of binary systems. We instead have chosen extrinsic parameters away from the extremes of parameter space. This means sky-locations that are away from nulls in any detector’s response, and inclinations ( $\iota \sim \pi/3$ ) that were not edge- or face-on with respect to the observer’s line of sight.

One of the more interesting results from this study is the impact of the subdominant modes on the parameter-estimation capabilities of ground-based detectors. The role that the additional modes play in the waveform depends heavily on both the mass ratio and the orientation of the binary — edge-on systems have the largest contribution from the additional modes, while face-on systems are most dominated by the (2,2) mode. It is therefore possible that, for some more extreme orientations, systematic biases could become large due to the increased importance of the additional modes.

To allay this concern we performed a series of MCMC runs on a system where the subdominant modes would

play an important role, exploring the edges of orientation space for each run. We chose the  $M = 120M_\odot$ ,  $q = 6$  system (row 8 in Tables I and II) and analyzed three different orientations: edge-on ( $\iota = \pi/2$ ), face-on ( $\iota = 0$ ), and moderate tilt ( $\iota = \pi/3$ ). We compare the  $\Delta \ln M$  and  $\Delta \ln \mathcal{M}$  posteriors for each of these systems using the  $\text{EOB}_{\text{HH}}$  model as a template to study data containing an NR waveform injected at SNR = 12. The results in

$\iota$	$\sigma_{\ln M}$	$\delta\beta_{\ln M}$	$\sigma_{\ln \mathcal{M}}$	$\delta\beta_{\ln \mathcal{M}}$	%MR	%HH
0	0.03	0.10	0.04	0.12	55	$\sim 0$
$\pi/3$	0.02	0.29	0.03	0.06	59	7.5
$\pi/2$	0.02	0.18	0.03	0.01	60	10

TABLE III: Fractional systematic errors and statistical errors for  $\ln M$  and  $\ln \mathcal{M}$  when  $M = 120M_\odot$ ,  $q = 6$ , SNR = 12 and for three different inclinations: Edge-on ( $\iota = \pi/2$ ), face-on ( $\iota = 0$ ), and an intermediate orientation ( $\iota = \pi/3$ ). We also include the percentage that the merger (MR) and additional modes (HH) contribute to the total SNR.

Table III show the fractional systematic error well below unity for each orientation regardless of the inclination angle. We also include the percentage of the total SNR that comes from the merger and ringdown of the waveform (MR) and the additional modes (HH). This result confirms that the parameter-estimation accuracy of the EOB model is robust to different orientations, and thus different strengths of the additional modes.

### D. Simulating a detection

All of the above results have been performed on simulated data that do not contain any noise, but do include the noise PSD in the inner product defined in Eq. (3). Thus the posteriors that we generate are not representative of a probability density function for an actual GW measurement, but instead are the hypothetical averaged measurements of the same system in an ensemble of noise realizations [69–71]. To more realistically demonstrate the parameter-estimation capabilities of advanced

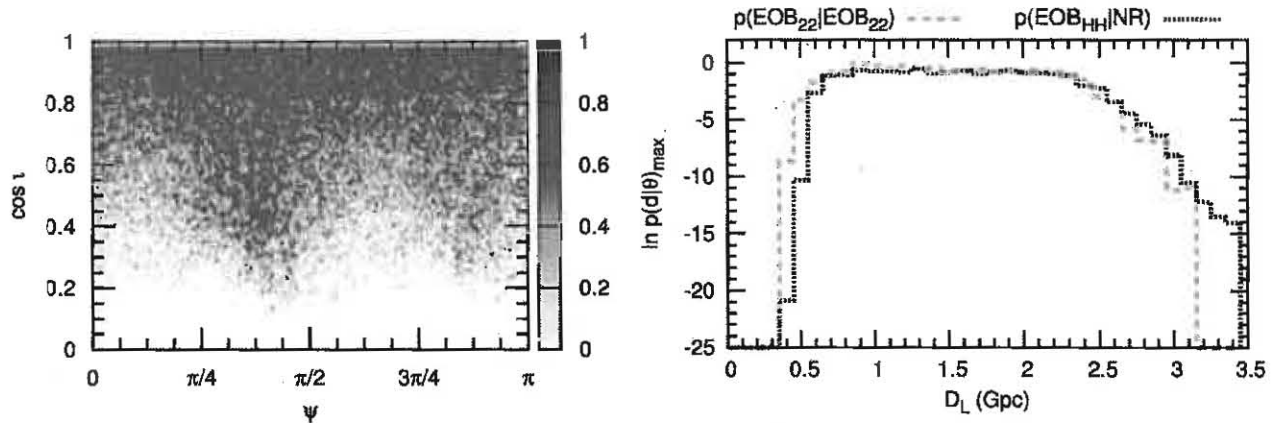


FIG. 3: Selected results from the  $q = 1$ ,  $\text{SNR} = 12$  run to exhibit the breakdown of  $\delta\beta$  as a useful statistic. The left-hand panel shows the 2D marginalized posterior for the orientation angles  $\psi$  and  $\cos i$ , with darker colors corresponding to higher probability density. The right-hand panel displays the maximum logarithmic likelihood as a function of  $D_L$ , which is effectively uniform between  $\sim 0.5$  and  $\sim 2.25$  Gpc.

ground-based interferometers, we want now to simulate a single LIGO/Virgo detection.

To that end, we use again the binary configuration with  $q = 2$ ,  $M = 51M_\odot$  and network SNR of 12, but now add stationary, gaussian noise to the NR waveform using the same PSD as in the noise-free study. The resultant posteriors are then representative parameter-estimation products, subject to the following important caveats:

- We use the same PSD for each detector when, in practice, each interferometer will have different sensitivity at any given time. Furthermore, the Virgo design sensitivity is not identical to LIGO (although it is qualitatively similar). We also effectively introduce a noise “wall” at 30 Hz to account for the limited duration of the NR data.
- We do not include any calibration errors in the waveform injections, which could prove to be a significant contribution to the overall parameter-estimation error budget [72]. Furthermore, we do not account for intrinsic error in the NR waveforms.
- We recognize that simulated additive gaussian noise is different from injecting waveforms into real LIGO/Virgo noise [56].

For this study we find the 2D marginalized posterior distribution functions to be of the most interest. We show results for the sky-location in Fig. 4 and mass parameters in Figs. 5 and 6.

In Fig. 4, the sky-location posterior is shown in a Molweide projection with the detector locations projected on to the celestial sphere. The white, dotted lines show the circles of constant time delay between each pair of detectors. The posterior should sit at intersections, and the principal axis should lie along a line. A small white square is included, centered on the injected position. The

injected values for the sky location are contained within the  $\sim 63\%$  confidence interval of the posterior (the red region of the error ellipse). The injected sky location was chosen to be a region where the SNR in each detector was roughly equivalent.

Of more pertinence to this study are the mass posteriors. While  $\ln M$  and  $\ln \mathcal{M}$  are the most convenient parameters for the MCMC sampler, being the most orthogonal, they are not of the most interest to the wider astrophysical community. A better data product would be posteriors on either the individual masses  $m_1$  and  $m_2$ , or the total mass and mass ratio. In post-processing we take the MCMC chains and compute the relevant mass parameters at each step in the chain. The injected component black holes have masses  $m_1 = 34M_\odot$  and  $m_2 = 17M_\odot$ . We show the 2D marginalized posterior distribution functions for the  $m_1$ - $m_2$  (Fig. 5), and  $M$ - $q$  plane (Fig. 6), where the color corresponds to the posterior density.

These figures give a good depiction of just how correlated the mass parameters are with one another, and how much of parameter space is supported by the chain in part due to that strong correlation. For example, the  $M$ - $q$  plane has significant support for mass ratios between 1 and 3, compatible with previous LIGO MCMC studies using PN waveforms (e.g., see Ref. [48]). These are the type of parameter-estimation products that the astrophysics community can anticipate as the advanced detectors come on line in the coming years.

## V. RESULTS FOR SPACE-BASED DETECTORS

For EOB waveforms that include subdominant modes, we have found relatively small systematic errors in parameter-estimation results for ground-based observations with  $\text{SNR} < 50$ . Because ground-based GW instru-

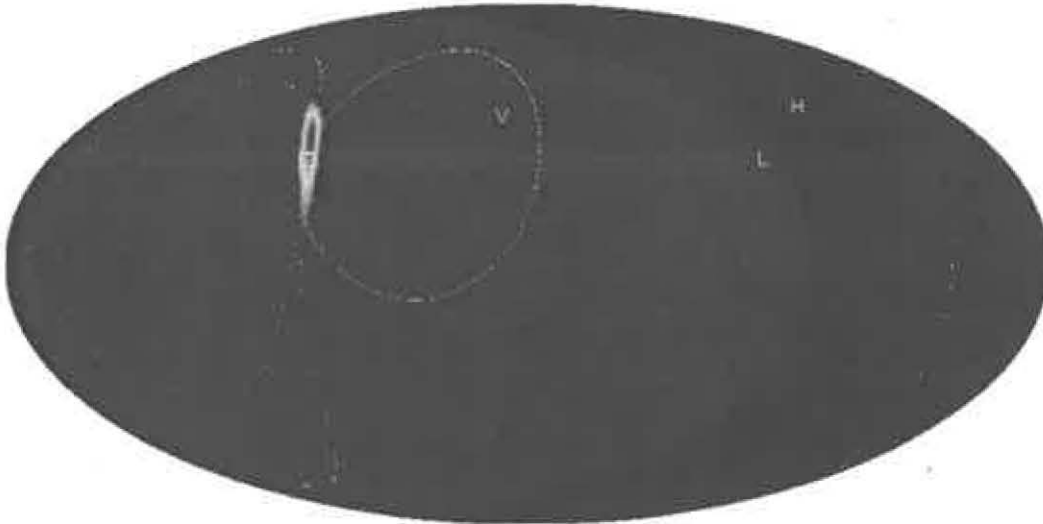


FIG. 4: 2D marginalized posterior distribution function for the sky-location of a  $q = 2$ ,  $M = 50M_{\odot}$ , binary with  $\text{SNR} = 12$  injected into simulated stationary gaussian noise colored by the Advanced LIGO noise power spectral density. The red, yellow, and cyan regions roughly correspond to  $1$ ,  $2$ , and  $3\sigma$  confidence regions. The white box represents the injected sky location of this source. The position of each interferometer in the network are projected onto the sky, and depicted with H, L, and V for LIGO Hanford, LIGO Livingston, and Virgo. The white, dashed lines show the locations that yield the same time-delay between each pair of detectors for the injected sky position.

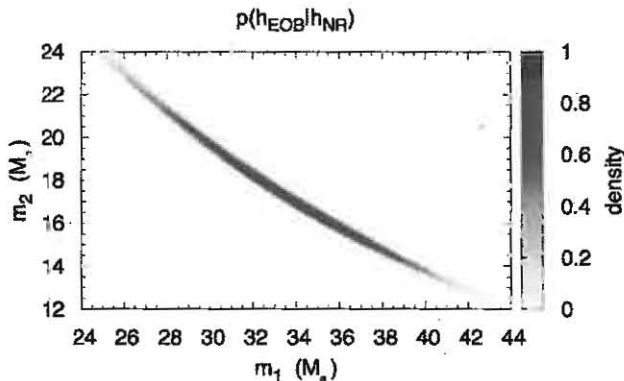


FIG. 5: 2D marginalized posterior distribution function for the individual masses  $m_1$  and  $m_2$  of a  $q = 2$ ,  $M = 51M_{\odot}$ , binary with  $\text{SNR} = 12$ , injected into simulated stationary gaussian noise colored by the Advanced LIGO noise power spectral density. The injected values for  $\{m_1, m_2\}$  were  $\{34, 17\}M_{\odot}$ .

ment rates are limited by sensitivity, higher-SNR events are exceedingly unlikely in the first generation of detections. Proposed space-based instruments will be sensitive to supermassive black-hole (SMBH) mergers out to cosmological scales, such that a significant fraction of detected events may have  $\text{SNR} > 100$ . Space-based instruments are typically sensitive to these events over a broad bandwidth covering a large number of cycles leading up to merger [4, 73]. Such observations will make

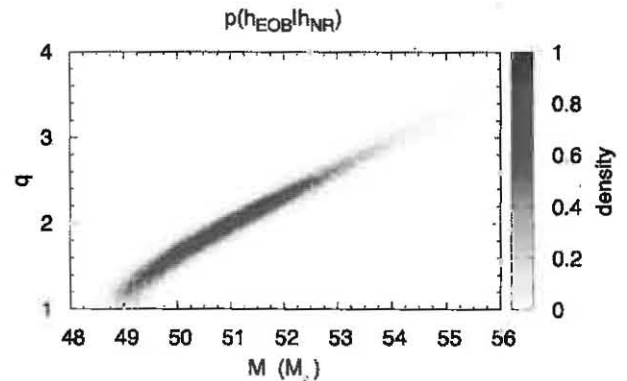


FIG. 6: Same as Fig. 5, but now depicting total mass  $M$  and mass ratio  $q$ .

much greater demands on the accuracy and efficiency of inspiral-merger-ringdown waveform templates. Though considerable effort has gone into estimating the ability of space-based instruments to measure astrophysical parameters assuming accurate waveforms, very little has been done to assess the template requirements for these future observations. Here we make a limited exploration of the capability with the current numerical-relativity and EOB waveforms to pursue space-based observations.

Of several proposed space-based GW interferometer instruments [3, 4, 74, 75], the best studied concept is the classic LISA mission [3]. While acknowledging that

there is currently considerable uncertainty about when and how the first space-based GW instrument will be developed, we choose to study the classic LISA configuration to make contact with the large body of work that has already been dedicated to black-hole merger parameter estimation (e.g., see Refs. [30, 31, 76–78]). To compare with other concepts, the most relevant alteration from the classic LISA design is the arm-length (e.g., from 5 Gm for classic LISA down to 1 Gm for eLISA), which sets the overall scale for parameter-estimation capabilities. Our results for a more modest detector configuration would be very similar to those for classic LISA, after appropriately rescaling the total mass of the black-hole system.

We follow here the same procedure outlined for the LIGO/Virgo studies in Sec. IV, where NR waveforms are injected into simulated noise-free data, and the signals are analyzed using the EOB model as a template. Because we saw significant bias in the EOB<sub>22</sub> model at SNR  $\sim 50$  it is safe to assume that those errors will only grow with SNR, and so we focus these runs only on the EOB<sub>HH</sub> model.

The duration of the available NR data restricts us to brief LISA observations, for which we can apply the static limit for the detector; thus we neglect LISA’s orbital motion during the observation time. Consistently, we focus on systems of mass  $3 \times 10^7 M_\odot$  at the high end of LISA’s sensitive range. For such observations the maximum frequency attained by the merger signal is well below the transfer frequency of the detector (when the wavelength of the GW signal is comparable to the size of the detector). In this low-frequency, static regime, the instrument response is equivalent to two  $60^\circ$  Michelson interferometers, co-located, and misaligned by  $\pi/3$  radians. The antenna patterns for this configuration, and the discussion of the two limits applied here, can be found in Ref. [79].

We consider mass-ratios in the range  $2 \leq q \leq 6$  observed at SNR=100, which would make these unusually distant for LISA observations. As shown in Fig. 7, the power-spectral density is similar over this mass-ratio range with more structure at  $q = 6$ . The noise-weighted waveforms for these cases are most comparable to the largest-mass  $120M_\odot$  LIGO case that we studied. Space-based instruments are not expected to have a strong power-law slope like the seismic noise wall in the LIGO sensitivity curve, meaning that even for large masses there is a softer degradation of sensitivity going back to the early portions of the signal, making our  $f_{\min}$  cut somewhat more artificial here.

Generally the higher SNRs of our nominal LISA observations would predict larger bias from systematic errors in the template waveforms. Because of the differences between the sensitivity curves and response for LISA and LIGO, however, it is not straightforward to scale up such expectations. Table IV shows our results for the parameter biases for mass  $M$  and chirp mass  $\mathcal{M}$ . Unlike the LIGO results, the biases here are already significant in most cases for LISA observations at SNR=100, reaching

a few times the statistical error level. In Table IV we also provide the SNR of the residuals after the MAP waveforms are removed from the data. These residuals with SNR  $> 6$  would be detectable and could therefore lead to biases in estimates of overlapping signals. Residuals at this level would also limit the utility of the current waveform templates for studies aimed at testing general relativity [52, 53].

For LISA, however, such a system would have to be exceedingly distant, at redshift  $z > 20$  or more, in order to expect an SNR as small as 100 [78]. Actual SNRs could be as much as 100 times larger, and we would expect correspondingly larger relative biases and residuals. Full interpretation of LISA data would thus require higher levels of template accuracy. Even the level of errors in the numerical simulations used here in place of the exact predictions of general relativity are far too large to avoid biasing such high-SNR measurements.

That being said, while the statistical error should decrease linearly with increasing SNR (causing  $\delta\beta$  to grow), the systematic error should remain approximately the same, and the absolute biases in the mass parameters are small. Reading from Table IV we see that the systematic errors in  $M$  and  $\mathcal{M}$  are  $\lesssim 1\%$ . Converting these into the individual masses, the biases on  $m_1$  and  $m_2$  are at most a few percent. While the MAP mass parameters may end up many  $\sigma$  away from the true values and would thus fall short of an optimal analysis of LISA data, such  $\sim 1\%$  errors in the masses are still small in astrophysical terms and may have little impact on key inferences made about the massive black-hole population. For example, when trying to constrain black-hole formation scenarios using simulated eLISA BBH catalogs, Amaro-Seoane et al [4] (based on the procedure in Ref. [51]) endured statistical errors as high as  $\sim 1\%$  and were still able to easily discriminate between black hole seed models.

The limitations of our current analysis prevent us from providing any detailed indication of how far template accuracy must be improved for space-based observations. For the detector configuration used here, the *extrinsic* parameter estimation at SNR = 100 is actually worse than that for the ground-based detectors. Space-based detectors rely on the long duration of the signals, the amplitude and Doppler modulations caused by the orbital motion, and finite-arm-length effects, to break degeneracies among the system parameters. We are limited here to working in a regime where all of those features are missing from our instrument model, so our classic LISA response is more like a two-detector co-located LIGO network operating at significantly lower frequencies than the existing ground-based detectors.

More complete analysis will require either dramatically longer-duration numerical simulations or a suitably well-controlled way of matching analytical and NR waveforms at low frequency that does not add as much systematic error as the template models being tested. We would also require more computationally efficient signal generation to successfully study template biases with long-duration

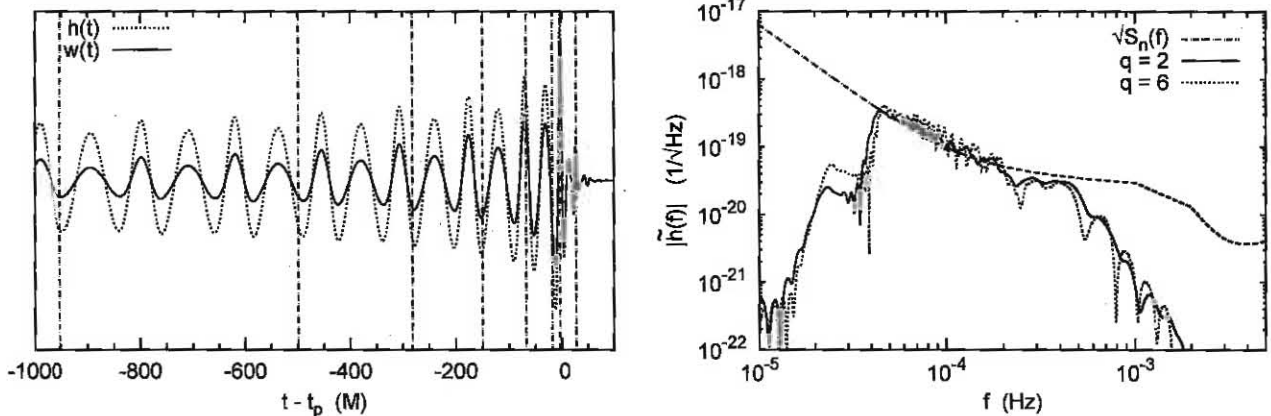


FIG. 7: Same as Fig. 1 now showing the LISA examples using  $M = 3 \times 10^7 M_\odot$  at  $\text{SNR} = 100$ . The time-domain waveform in the left-hand panel is for the  $q = 6$  case.

$q$	$M (M_\odot)$	$f_{\text{low}} (\text{Hz})$	SNR	$p(\text{EOB}_{\text{HH}} \text{EOB}_{\text{HH}})$					$p(\text{EOB}_{\text{HH}} \text{NR})$				
				$\sigma_{\ln M}$	$\sigma_{\ln \mathcal{M}}$	$\delta\beta_{\ln M}$	$\delta\beta_{\ln \mathcal{M}}$	$\text{SNR}_{\text{res}}$	$\sigma_{\ln M}$	$\sigma_{\ln \mathcal{M}}$	$\delta\beta_{\ln M}$	$\delta\beta_{\ln \mathcal{M}}$	$\text{SNR}_{\text{res}}$
2	$3 \times 10^7$	$5 \times 10^{-5}$	100	$2 \times 10^{-3}$	$2 \times 10^{-3}$	0.09	0.08	0.5	$2 \times 10^{-3}$	$2 \times 10^{-3}$	1.19	1.27	6.5
3	$3 \times 10^7$	$5 \times 10^{-5}$	100	$2 \times 10^{-3}$	$3 \times 10^{-3}$	0.02	0.04	0.7	$3 \times 10^{-3}$	$2 \times 10^{-3}$	0.59	2.82	7.7
4	$3 \times 10^7$	$5 \times 10^{-5}$	100	$3 \times 10^{-3}$	$2 \times 10^{-3}$	0.10	0.09	0.5	$3 \times 10^{-3}$	$3 \times 10^{-3}$	1.31	3.02	9.6
6	$3 \times 10^7$	$5 \times 10^{-5}$	100	$2 \times 10^{-3}$	$2 \times 10^{-3}$	0.16	0.27	0.5	$3 \times 10^{-3}$	$2 \times 10^{-3}$	0.62	0.92	11.5

TABLE IV: Same as Table I but for SMBH mergers as seen by LISA. Here we also include the residual SNR after the MAP waveform is regressed from the data. The  $p(\text{EOB}|\text{EOB})$  study used the  $\text{EOB}_{\text{HH}}$  model for each example.

waveforms.

## VI. CONCLUSIONS AND DISCUSSION

In this paper, we have produced the first measurement of systematic errors introduced by using EOB templates to analyze NR waveforms. Our study's main focus was on stellar-mass BBHs observed by Advanced LIGO and Virgo. We also considered massive black-hole mergers detectable by space-based interferometers like LISA. We have injected NR waveforms into simulated data and have used an MCMC sampler to characterize the posterior distribution function for the astrophysical parameters. Our metric for assessing the size of the systematic error is to compare the offset between the injected and best-fit parameters to the statistical error characterized by the standard deviation of the 1D marginalized posteriors.

Several of our examples were chosen specifically to compare with Fig. 15 in Ref. [25]. Encouragingly, we find that the EOB waveforms accurately recover binary parameters at SNRs higher than were predicted in Ref. [25] using the (deliberately) conservative accuracy requirements of Refs. [40, 41].

For the stellar-mass systems we have investigated, when including the subdominant modes, we find system-

atic biases consistently comparable to, or smaller than, the statistical errors for mass ratios up to  $q = 6$  and SNRs  $\lesssim 50$ . We have tested these waveforms in the most stringent way possible, simulating high-SNR events where the merger (the least reliable part of the waveform calculations) is peaking in the most sensitive band of the detector, and the higher-frequency modes contribute significantly to the overall signal power. For the  $q = 6$  waveforms, the fraction of power contained in the subdominant modes is 11% and 16% for the  $M = 56 M_\odot$  and  $M = 120 M_\odot$  systems, respectively. We also tested low-mass systems ( $M \sim 20 M_\odot$ ) to better represent likely Advanced LIGO/Virgo detections. In all of these examples, the bias introduced by the EOB waveform in Ref. [25] was *at worst* comparable to the statistical errors.

Matched-filtering analyses are most sensitive to the phase of the signal, and it is the phase of the waveform that is most influenced by different choices of model. It is therefore predictable that the most significant biases appear in the mass parameters. On the other hand, the extrinsic parameters have comparatively less impact on the shape of the signal — the distance comes in as an overall amplitude scaling, and the sky location is (for ground-based interferometers) predominantly determined through triangulation based on time delays between detectors. Therefore a model waveform used for parameter estimation has much more room for error if,

for instance, the location of the binary is the primary interest (say, for optical counterpart searches) and the requirements on the phase-matching are not as severe.

While the results here are undoubtedly positive, there is still work to be done in waveform modeling. We are only testing the EOB waveforms over the last 30–40 GW cycles before merger and there is no guarantee that longer waveforms will not accumulate larger phase errors during the early portion of the inspiral. Furthermore, this study leaves off significant aspects of the waveform structure related to black-hole spins and orbital eccentricity. A similar study will need to be performed with long-duration, spinning systems once both the NR and EOB waveforms are prepared for that test. It will also be valuable to test the EOB waveforms over a broader class of NR simulations, including those that were not used to calibrate the template model. Moreover, we have assumed in this paper that the NR waveforms were exact but, as discussed in Sec. II, this is not the case. One possibility for taking the numerical error into account is to inject NR waveforms computed at different resolution and/or extracted at different radii and measure the EOB systematic biases in each case. The difference between these biases can provide us with an estimate of the intrinsic error caused by the NR waveforms deviating from the exact solution in general relativity. Finally, we do not consider the effects of real detector noise or calibration errors in the data, both of which could prove to be a significant contribution to the overall error budget [56, 72].

While EOB waveforms that include subdominant modes were found to have relatively small systematic errors in parameter-estimation results for ground-based observations with  $\text{SNR} < 50$ , proposed space-based instruments are sensitive to SMBH mergers with  $\text{SNR} > 100$ . For these scenarios, we find statistically significant biases in the mass parameters for mass-ratios in the range  $2 \leq q \leq 6$  observed at  $\text{SNR} = 100$ , on the order of  $\sim 1\%$

for the component masses of the system. However, as discussed in Sec. V, systematic errors introduced by the EOB templates are small enough to still place strong constraints on the population of massive black holes in the Universe.

In the LISA examples, the residual power exceeded the  $\text{SNR} > 6$  threshold above which the data analysis could be compromised both in parameter estimation of overlapping signals and studies aimed at testing general relativity. Space-based GW data analysis will require more accurate templates grounded in even more accurate numerical simulations.

A more complete analysis is needed, but will require either dramatically longer-duration numerical simulations or a suitably well-controlled way of matching analytical and NR waveforms at low frequency. We would also require more computationally efficient signal generation to successfully study template biases with long-duration waveforms.

## VII. ACKNOWLEDGMENTS

We would like to thank Ryan Lang, Sean McWilliams, Yi Pan, Ira Thorpe for very useful discussions. We also thank the Caltech-Cornell-CITA collaboration for providing us with the NR waveforms used in this work.

The authors acknowledge support from the NASA Grants 08-ATFP08-0126, 11-ATP11-0046, J.B and B.K. also acknowledge support from 09-ATP09-0136. A.B. also acknowledges support from the NSF Grants No. PHY-0903631 and PHY-1208881.

The MCMC runs were carried out using resources from the NASA Center for Computational Sciences at Goddard Space Flight Center, and the Nemo cluster supported by National Science Foundation awards PHY-0923409 and PHY-0600953 to UW-Milwaukee.

- 
- [1] B. Abbott et al. (LIGO Scientific Collaboration), Rept. Prog. Phys. **72**, 076901 (2009), arXiv:0711.3041 [gr-qc].
  - [2] T. Accadia, F. Acernese, F. Antonucci, P. Astone, G. Ballardin, et al., Class. Quantum Grav. **28**, 114002 (2011).
  - [3] O. Jennrich, Class. Quantum Grav. **26**, 153001 (2009), arXiv:0906.2901 [astro-ph.IM].
  - [4] P. Amaro-Seoane et al. (2012), arXiv:1201.3621 [astro-ph.CO].
  - [5] G. Hobbs, A. Archibald, Z. Arzoumanian, D. Backer, M. Bailes, et al., Class. Quantum Grav. **27**, 084013 (2010), arXiv:0911.5206 [astro-ph.SR].
  - [6] M. Sasaki and H. Tagoshi, Living Rev. Rel. **6**, 6 (2003), arXiv:gr-qc/0306120.
  - [7] L. Blanchet, Living Rev. Rel. **9**, 4 (2006).
  - [8] T. Futamase and Y. Itoh, Living Rev. Rel. **10**, 2 (2007).
  - [9] W. D. Goldberger and I. Z. Rothstein, Phys. Rev. D **73**, 104029 (2006), arXiv:hep-th/0409156.
  - [10] F. Pretorius, Phys. Rev. Lett. **95**, 121101 (2005), arXiv:gr-qc/0507014.
  - [11] M. Campanelli, C. Lousto, P. Marronetti, and Y. Zlochower, Phys. Rev. Lett. **96**, 111101 (2006), arXiv:gr-qc/0511048.
  - [12] J. G. Baker, J. Centrella, D.-I. Choi, M. Koppitz, and J. van Meter, Phys. Rev. Lett. **96**, 111102 (2006), arXiv:gr-qc/0511103.
  - [13] C. V. Vishveshwara, Nature **227**, 936 (1970).
  - [14] S. Chandrasekhar and S. Detweiler, Proc. R. Soc. London Ser. A **344**, 441 (1975).
  - [15] A. Buonanno, G. B. Cook, and F. Pretorius, Phys. Rev. D **75**, 124018 (2007), arXiv:gr-qc/0610122.
  - [16] A. Buonanno et al., Phys. Rev. D **76**, 104049 (2007), arXiv:0706.3732 [gr-qc].
  - [17] Y. Pan, A. Buonanno, J. G. Baker, J. Centrella, B. J. Kelly, et al., Phys. Rev. D **77**, 024014 (2008), arXiv:0704.1964 [gr-qc].
  - [18] P. Ajith, S. Babak, Y. Chen, M. Hewitson, B. Krishnan, et al., Class. Quantum Grav. **24**, S689 (2007),

- arXiv:0704.3764 [gr-qc].
- [19] T. Damour and A. Nagar, *Phys. Rev. D* **77**, 024043 (2008), arXiv:0711.2628 [gr-qc].
- [20] T. Damour and A. Nagar, *Phys. Rev. D* **79**, 081503 (2009), arXiv:0902.0136 [gr-qc].
- [21] P. Ajith, M. Hannam, S. Husa, Y. Chen, B. Bruegmann, et al., *Phys. Rev. Lett.* **106**, 241101 (2011), arXiv:0909.2867 [gr-qc].
- [22] Y. Pan et al., *Phys. Rev. D* **81**, 084041 (2010), arXiv:0912.3466 [gr-qc].
- [23] L. Santamaria, F. Ohme, P. Ajith, B. Bruegmann, N. Dorband, et al., *Phys. Rev. D* **82**, 064016 (2010), arXiv:1005.3306 [gr-qc].
- [24] R. Sturani, S. Fischetti, L. Cadonati, G. Guidi, J. Healy, et al., *J. Phys. Conf. Ser.* **243**, 012007 (2010), arXiv:1005.0551 [gr-qc].
- [25] Y. Pan, A. Buonanno, M. Boyle, L. T. Buchman, L. E. Kidder, et al., *Phys. Rev. D* **84**, 124052 (2011), arXiv:1106.1021 [gr-qc].
- [26] A. Taracchini, Y. Pan, A. Buonanno, E. Barausse, M. Boyle, et al., *Phys. Rev. D* **86**, 024011 (2012), 1202.0790.
- [27] J. Abadie et al. (LIGO Scientific Collaboration, Virgo Collaboration), *Phys. Rev. D* **83**, 122005 (2011), arXiv:1102.3781 [gr-qc].
- [28] J. Abadie et al. (LIGO Scientific Collaboration, Virgo Collaboration) (2012), arXiv:1201.5999 [gr-qc].
- [29] P. Ajith and S. Bose, *Phys. Rev. D* **79**, 084032 (2009), arXiv:0901.4936 [gr-qc].
- [30] S. T. McWilliams, B. J. Kelly, and J. G. Baker, *Phys. Rev. D* **82**, 024014 (2010), arXiv:1004.0961 [gr-qc].
- [31] S. T. McWilliams, R. N. Lang, J. G. Baker, and J. I. Thorpe, *Phys. Rev. D* **84**, 064003 (2011), arXiv:1104.5650 [gr-qc].
- [32] A. Buonanno and T. Damour, *Phys. Rev. D* **59**, 084006 (1999), arXiv:gr-qc/9811091.
- [33] A. Buonanno and T. Damour, *Phys. Rev. D* **62**, 064015 (2000), arXiv:gr-qc/0001013.
- [34] T. Damour, P. Jaranowski, and G. Schaefel, *Phys. Rev. D* **62**, 084011 (2000), arXiv:gr-qc/0005034.
- [35] T. Damour, *Phys. Rev. D* **64**, 124013 (2001), arXiv:gr-qc/0103018.
- [36] A. Buonanno, Y. Chen, and T. Damour, *Phys. Rev. D* **74**, 104005 (2006), arXiv:gr-qc/0508067.
- [37] P. Canitrot, *Phys. Rev. D* **63**, 082005 (2001).
- [38] C. Cutler and M. Vallisneri, *Phys. Rev. D* **76**, 104018 (2007), arXiv:0707.2982 [gr-qc].
- [39] S. Bose, A. Gopakumar, and M. Tessmer (2008), arXiv:0807.2400 [gr-qc].
- [40] L. Lindblom, *Phys. Rev. D* **80**, 064019 (2009), arXiv:0907.0457 [gr-qc].
- [41] L. Lindblom, J. G. Baker, and B. J. Owen, *Phys. Rev. D* **82**, 084020 (2010), arXiv:1008.1803 [gr-qc].
- [42] N. Metropolis, A. Rosenbluth, R. M.N., A. Teller, and E. Teller, *J. Chem. Phys.* **21**, 1087 (1953).
- [43] W. Hastings, *Biometrika* **57**, 97 (1970).
- [44] L. T. Buchman, H. P. Pfeiffer, M. A. Scheel, and B. Szilagyi (2012), arXiv:1206.3015 [gr-qc].
- [45] A. Vecchio, *Phys. Rev. D* **70**, 042001 (2004), arXiv:0304051 [astro-ph].
- [46] E. Berti, A. Buonanno, and C. M. Will, *Phys. Rev. D* **71**, 084025 (2005), arXiv:0411129 [gr-qc].
- [47] R. N. Lang and S. A. Hughes (2007), arXiv:0710.3795 [astro-ph].
- [48] M. van der Sluys, C. Roever, A. Stroeer, N. Christensen, V. Kalogera, et al. (2007), arXiv:0710.1897 [astro-ph].
- [49] K. Arun, S. Babak, E. Berti, N. Cornish, C. Cutler, et al., *Class. Quantum Grav.* **26**, 094027 (2009), arXiv:0811.1011 [gr-qc].
- [50] J. E. Plowman, D. C. Jacobs, R. W. Hellings, S. L. Larson, and S. Tsuruta (2009), arXiv:0903.2059 [astro-ph.CO].
- [51] A. Sesana, J. Gair, E. Berti, and M. Volonteri, *Phys. Rev. D* **83**, 044036 (2011), arXiv:1011.5893 [astro-ph.CO].
- [52] T. Li, W. Del Pozzo, S. Vitale, C. Van Den Broeck, M. Agathos, et al., *Phys. Rev. D* **85**, 082003 (2012), 1110.0530.
- [53] M. Vallisneri (2012), arXiv:1207.4759 [gr-qc].
- [54] E. Barausse, A. Buonanno, S. A. Hughes, G. Khanna, S. O'Sullivan, et al., *Phys. Rev. D* **85**, 024046 (2012), arXiv:1110.3081 [gr-qc].
- [55] *LSC Algorithm Library suite*, <https://www.lsc-group.phys.uwm.edu/daswg/projects/la suite.html>.
- [56] V. Raymond, M. van der Sluys, I. Mandel, V. Kalogera, C. Rover, et al., *Class. Quantum Grav.* **27**, 114009 (2010), arXiv:0912.3746 [gr-qc].
- [57] J. Abadie et al. (LIGO Scientific Collaboration, Virgo Collaboration), *Phys. Rev. D* **82**, 102001 (2010), arXiv:1005.4655 [gr-qc].
- [58] R. Swendsen and J. Wang, *Phys. Rev. Lett.* **57**, 2607 (1986).
- [59] C. J. Ter Braak, *Statistics and Computing* **16**, 239 (2006).
- [60] N. J. Cornish and J. Crowder, *Phys. Rev. D* **72**, 043005 (2005), arXiv:gr-qc/0506059.
- [61] LIGO-T0900288-v3 (2010), URL <https://dcc.ligo.org/cgi-bin/DocDB/ShowDocument?docid=2974>.
- [62] W. Anderson, P. Brady, D. Chin, J. Creighton, K. Riles, and J. Whelan, *Beam pattern response functions and times of arrival for earthbound interferometer*, LIGO-T010110-00-Z (2001).
- [63] A. Prestwich, R. Kilgard, P. Crowther, S. Carpano, A. Pollock, et al., *Astrophys. J.* **669**, L21 (2007), arXiv:0709.2892 [astro-ph].
- [64] J. M. Silverman and A. V. Filippenko, *Astrophys. J.* **678**, L17 (2008), arXiv:0802.2716 [astro-ph].
- [65] K. Belczynski, T. Bulik, C. L. Fryer, A. Ruitter, J. S. Vink, et al., *Astrophys. J.* **714**, 1217 (2010), arXiv:0904.2784 [astro-ph.SR].
- [66] P. A. Crowther, O. Schnurr, R. Hirschi, N. Yusof, R. J. Parker, et al., *Mon. Not. Roy. Astron. Soc.* **308**, 731 (2010), arXiv:1007.3284 [astro-ph.SR].
- [67] C. Cutler, T. A. Apostolatos, L. Bildsten, L. S. Finn, E. E. Flanagan, et al., *Phys. Rev. Lett.* **70**, 2984 (1993), arXiv:astro-ph/9208005.
- [68] J. Veitch, I. Mandel, B. Aylott, B. Farr, V. Raymond, et al., *Phys. Rev. D* **85**, 104045 (2012), arXiv:1201.1195 [astro-ph.HE].
- [69] S. Nissanke, D. E. Holz, S. A. Hughes, N. Dalal, and J. L. Sievers, *Astrophys. J.* **725**, 496 (2010), arXiv:0904.1017 [astro-ph.CO].
- [70] N. Cornish, L. Sampson, N. Yunes, and F. Pretorius, *Phys. Rev. D* **84**, 062003 (2011), arXiv:1105.2088 [gr-qc].
- [71] M. Vallisneri, *Phys. Rev. Lett.* **107**, 191104 (2011), arXiv:1108.1158 [gr-qc].
- [72] S. Vitale, W. Del Pozzo, T. G. Li, C. Van Den Broeck, I. Mandel, et al., *Phys. Rev. D* **85**, 064034 (2012), arXiv:1111.3044 [gr-qc].

- [73] T. Prince et al., Tech. Rep., LISA International Science Team (2009), URL [http://list.caltech.edu/lib/exe/fetch.php?media=documents:science:lisa\\_science\\_case\\_v1\\_2.pdf](http://list.caltech.edu/lib/exe/fetch.php?media=documents:science:lisa_science_case_v1_2.pdf).
- [74] K. Anderson, R. T. Stebbins, R. Weiss, E. Wright, et al., Tech. Rep., NASA Physics of the Cosmos Program (2012), URL [http://pcos.gsfc.nasa.gov/physpag/GW\\_Study\\_Rev3\\_Aug2012-Final.pdf](http://pcos.gsfc.nasa.gov/physpag/GW_Study_Rev3_Aug2012-Final.pdf).
- [75] S. Kawamura et al., J. Phys. Conf. Ser. **122**, 012006 (2008).
- [76] E. Berti, J. Cardoso, V. Cardoso, and M. Cavaglia, Phys. Rev. D **76**, 104044 (2007), arXiv:0707.1202 [gr-qc].
- [77] J. Thorpe, S. McWilliams, B. Kelly, R. Fahey, K. Arnaud, et al., Class. Quantum Grav. **26**, 094026 (2009), arXiv:0811.0833 [astro-ph].
- [78] S. T. McWilliams, J. I. Thorpe, J. G. Baker, and B. J. Kelly, Phys. Rev. D **81**, 064014 (2010), arXiv:0911.1078 [gr-qc].
- [79] N. J. Cornish and L. J. Rubbo, Phys. Rev. D **67**, 022001 (2003), arXiv:gr-qc/0209011.